nature materials

LETTERS

PUBLISHED ONLINE: 27 SEPTEMBER 2009 | DOI: 10.1038/NMAT2542

MgZnCa glasses without clinically observable hydrogen evolution for biodegradable implants

Bruno Zberg[1], Peter J. Uggowitzer[1] and Jörg F. Löffler[1]*

Corrosion is normally an undesirable phenomenon in engineering applications. In the field of biomedical applications, however, implants that 'biocorrode' are of considerable interest. Deploying them not only abrogates the need for implant-removal surgery, but also circumvents the long-term negative effects of permanent implants[1]. In this context magnesium is an attractive biodegradable material, but its corrosion is accompanied by hydrogen evolution[2], which is problematic in many biomedical applications. Whereas the degradation and thus the hydrogen evolution of crystalline Mg alloys can be altered only within a very limited range, Mg-based glasses offer extended solubility for alloying elements plus a homogeneous single-phase structure, both of which may alter corrosion behaviour significantly[3,4]. Here we report on a distinct reduction in hydrogen evolution in Zn-rich MgZnCa glasses. Above a particular Zn-alloying threshold (≈28 at.%), a Zn- and oxygen-rich passivating layer forms on the alloy surface, which we explain by a model based on the calculated Pourbaix diagram of Zn in simulated body fluid. We document animal studies that confirm the great reduction in hydrogen evolution and reveal the same good tissue compatibility as seen for crystalline Mg implants. Thus, the glassy $Mg_{60+x}Zn_{35-x}Ca_5$ ($0 \le x \le 7$) alloys show great potential for deployment in a new generation of biodegradable implants.

Two material classes have been the focus of biodegradable applications: polymers and metals. Of the two, metallic materials show the greater mechanical strength, and metallic corrosion products provoke fewer inflammatory reactions[1]. Iron and magnesium alloys are possible candidates for use in cardiovascular intervention and osteosynthesis[2,5–9]. Whereas iron corrosion is very slow, magnesium alloys have appropriate corrosion rates in physiological media. Magnesium also shows a Young's modulus similar to that of bone ($E = 3$–20 GPa), which makes it particularly interesting for osteosynthesis applications. As early as the 1930s, feasibility studies showed the good resorbability and high biocompatibility level of magnesium bone-fixation implants[10–12]. However, they also reported the formation of unwanted, possibly harmful hydrogen gas pockets generated by the corrosion reaction $Mg + 2H_2O \rightarrow Mg^{2+} + 2OH^- + H_2$. Progress in alloy development, resulting mainly in new compositions and high-purity alloys, has produced an increased corrosion resistance and thus a reduced hydrogen-evolution rate[13]. The hydrogen evolution in filigree implants, such as cardiovascular stents, seems to be of minor importance; preclinical and clinical studies indicate good biocompatibility, with minimal inflammatory changes and complete absorption within two months[1,6,7,14,15]. In osteosynthesis applications, however, hydrogen evolution remains problematic. As a result of the increased Mg mass and poor transport mechanisms, gas pockets occur around these implants; in animal studies, subcutaneous gas bubbles have had to be removed by means of puncture procedures[2,5].

The corrosion of magnesium is strongly influenced by alloying elements in solid solution[4,16,17]. The solubility of alloying elements in crystalline Mg, however, is limited, that is, corrosion mechanisms can in principle be modified but not completely altered. Hydrogen evolution will thus remain a problem during the degradation of crystalline Mg alloys. In contrast, the potentially much greater range of alloying elements in an amorphous single-phase structure allows the production of particular metallic glasses with significantly improved corrosion characteristics[3]. This implies that glassy Mg alloys may exist for which hydrogen evolution during degradation is significantly reduced or even prevented completely. Furthermore, because there is no dislocation-based plastic-deformation mechanism in amorphous alloys, bulk metallic glasses[18–21] reveal greatly improved strength and elasticity (for typical compositions, see refs 22, 23). Various mechanical properties of MgZnCa glasses[24–26] are listed in Table 1 and compared with those of conventional (WE43) and newly developed (ZQCa3, ZK31; ref. 27) crystalline Mg alloys. Although they possess lower ductility, the MgZnCa glasses show a strength nearly three times, and an elastic limit nearly four times higher than those of crystalline Mg alloys, and their Young's modulus is similarly low despite the greater amounts of alloying elements. Thus, the combination of increased mechanical strength, greater corrosion resistance and the potential absence of hydrogen evolution during degradation makes certain glassy Mg alloy compositions very interesting materials for biodegradable implant applications.

The investigated glassy $Mg_{60+x}Zn_{35-x}Ca_5$ alloys[24] ($x = 0$, 3, 6, 7, 9, 12, 14, 15; all compositions are given in at.%) were prepared by melt-spinning to obtain thin ribbons of 50 μm in thickness, and copper mould injection-casting to obtain 0.5-mm-thick plates (for an overview of metallic glass production, see ref. 28). As shown in Fig. 1a, according to the hydrogen-evolution tests, increasing the Zn content generates a significant change in behaviour: the crystalline reference samples (Mg and $Mg_{98}Zn_2$) and the Zn-poor glassy alloys feature strong gas evolution during degradation in simulated body fluid (SBF) (for SBF composition, see ref. 29 and the Methods section), whereas the Zn-rich alloys form hardly any hydrogen, with a distinct drop in the gas volume between the two 'corrosion states' at a Zn content of around 28 at.%. Figure 1b,c shows the results of electrochemical impedance spectroscopy (EIS) tests, which can be used to characterize the various corrosion states. The Nyquist plots illustrate the characteristics of two samples that show different hydrogen-evolution behaviour. Whereas at high frequency it is mainly the impedance of the solution that is measured, the low-frequency regime reflects the impedance of the sample. The Zn-poor $Mg_{72}Zn_{23}Ca_5$ sample (Fig. 1b), which demonstrates strong hydrogen evolution, shows very low values for the real part

[1]Laboratory of Metal Physics and Technology, Department of Materials, ETH Zurich, Wolfgang-Pauli-Str. 10, 8093 Zurich, Switzerland.
*e-mail: joerg.loeffler@mat.ethz.ch.

Table 1 | Mechanical properties of MgZnCa glasses compared with those of conventional (WE43) and newly developed (ZQCa3, ZK31) crystalline Mg alloys.

Material	Strength (MPa)	Weibull modulus	Elastic limit (%)	Plasticity (%)	Young's modulus (GPa)
$Mg_{66}Zn_{30}Ca_4$ (bulk glass in compression)	716–854	26	2.0	<2	48
$Mg_{67}Zn_{28}Ca_5$ (glassy wire in tension)	675–894	20.6	2.0	4	48
WE43 (crystalline)	270	N/A	0.39	10	44
ZQCa3 (crystalline)	250	N/A	0.32	27	44
ZK31 (crystalline)	300	N/A	0.51	15	44

The strength of amorphous alloys corresponds to the fracture strength; the strength of crystalline alloys corresponds to the ultimate tensile strength. The data for $Mg_{66}Zn_{30}Ca_4$ were taken from ref. 25 and for $Mg_{67}Zn_{28}Ca_5$ from ref. 26; the Young's modulus of 48 GPa was measured for $Mg_{70}Zn_{25}Ca_5$ (see ref. 24). The data for WE43 were taken from data sheet 478 of Magnesium Elektron (www.magnesium-elektron.com) and the data for ZQCa3 and ZK31 were taken from ref. 27.

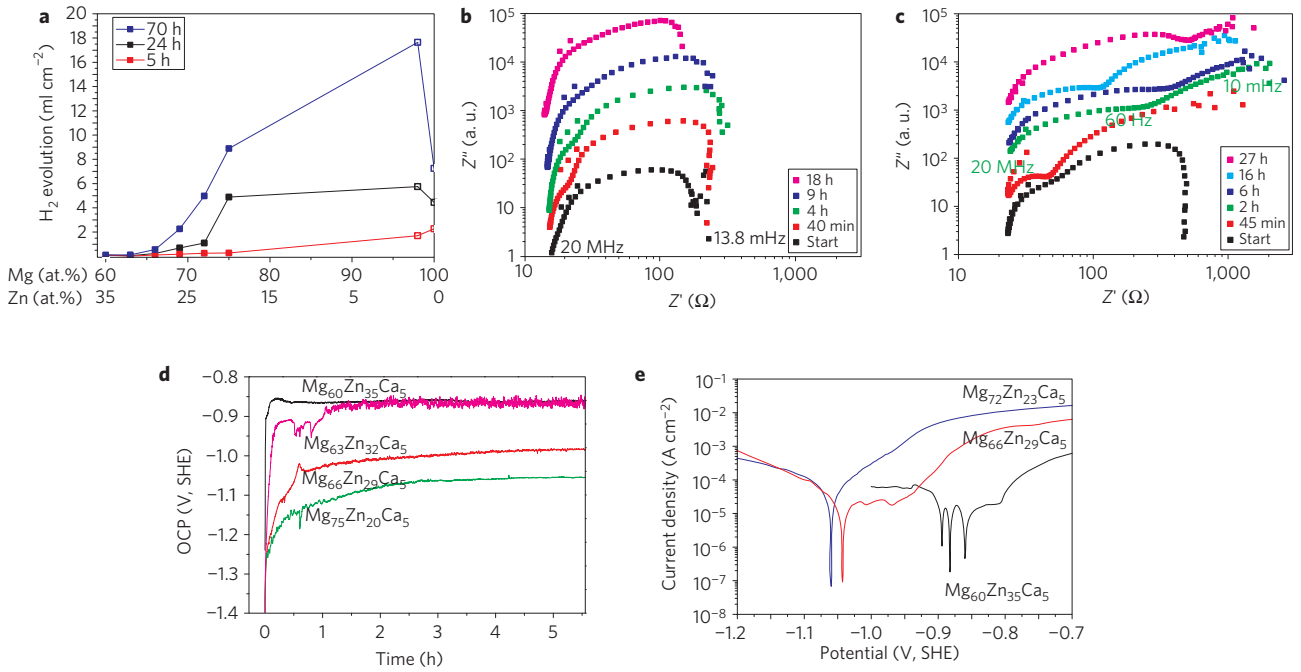

Figure 1 | Corrosion and electrochemical measurements of glassy MgZnCa alloys. a, Hydrogen-evolution measurements showing a distinct drop at high Zn content (filled symbols represent metallic glasses, open symbols represent crystalline reference alloys). **b**,**c**, Nyquist plots (where the imaginary part of the impedance is plotted versus its real part; here in a log–log representation) of glassy $Mg_{72}Zn_{23}Ca_5$ (**b**) and glassy $Mg_{60}Zn_{35}Ca_5$ (**c**). Whereas the Zn-poor MgZnCa glass shows only low impedance and one semicircle, the Zn-rich glass shows two semicircle-like shapes with fitted low-frequency impedances ranging from 3,000 to 5,000 Ω. **d**, Time dependence of the OCP with respect to SHE for various MgZnCa glasses. **e**, Passivation behaviour of $Mg_{60}Zn_{35}Ca_5$ and $Mg_{66}Zn_{29}Ca_5$ in comparison with $Mg_{72}Zn_{23}Ca_5$, which shows active corrosion behaviour. The OCP in **d** was measured with respect to SCE and then transferred to a potential difference with respect to SHE (U(SHE) = U(SCE) + 0.242 V), to make it comparable to the Pourbaix diagram in Fig. 2.

of the impedance at low frequencies; the impedance is at maximum 300 Ω after 4 h of immersion. This Zn-poor sample also shows an unchanging semicircle-like curve, indicating that similar corrosion processes have taken place over the whole immersion period. In comparison, the curve for the marginal-hydrogen-evolving, Zn-rich $Mg_{60}Zn_{35}Ca_5$ glass (Fig. 1c) changes drastically, from a single semicircle-like to a more complex two-semicircle-like shape. This indicates the activity of two processes with different time constants. The semicircle at higher frequencies is attributed to a rapid process similar to that observed in Fig. 1b, and is dominant at the start of the immersion experiment. The second semicircle at lower frequencies, which develops within approximately 45 min of immersion, points to an extra process with a slow charge transfer. This change in shape is accompanied by a significant increase in the real part of the impedance; fitting of the data at low frequencies indicates impedance values ranging from 3,000 to 5,000 Ω. The change in shape and the increase in corrosion resistance within the first 45 min indicate the build-up of surface conditions that are different from those of the $Mg_{72}Zn_{23}Ca_5$ glass. This is also supported by measurements of the open-circuit potential (OCP) of the immersed alloys. As can be seen in Fig. 1d, the two Zn-rich alloys ($Mg_{60}Zn_{35}Ca_5$ and $Mg_{63}Zn_{32}Ca_5$) show more noble (OCP versus standard hydrogen electrode (SHE) ≈ -0.85 V) and more rapidly stabilizing potentials than the Zn-poor $Mg_{75}Zn_{20}Ca_5$ glass with pronounced gas evolution. The $Mg_{66}Zn_{29}Ca_5$ is in an intermediate state. The increasing OCP after immersion indicates the growth of a corrosion layer. As a result of the differing OCPs, these layers are different for the Zn-poor and Zn-rich MgZnCa glasses, generating significant alterations in the corrosion behaviour (see below for more details). The changes in OCP are confirmed in potentiodynamic measurements (Fig. 1e), which also indicate a short passive corrosion plateau for the $Mg_{66}Zn_{29}Ca_5$ and $Mg_{60}Zn_{35}Ca_5$ glasses. The three zero crossings observed for the $Mg_{60}Zn_{35}Ca_5$ glass are generated by the kinetics of corrosion-product formation on the sample surface.

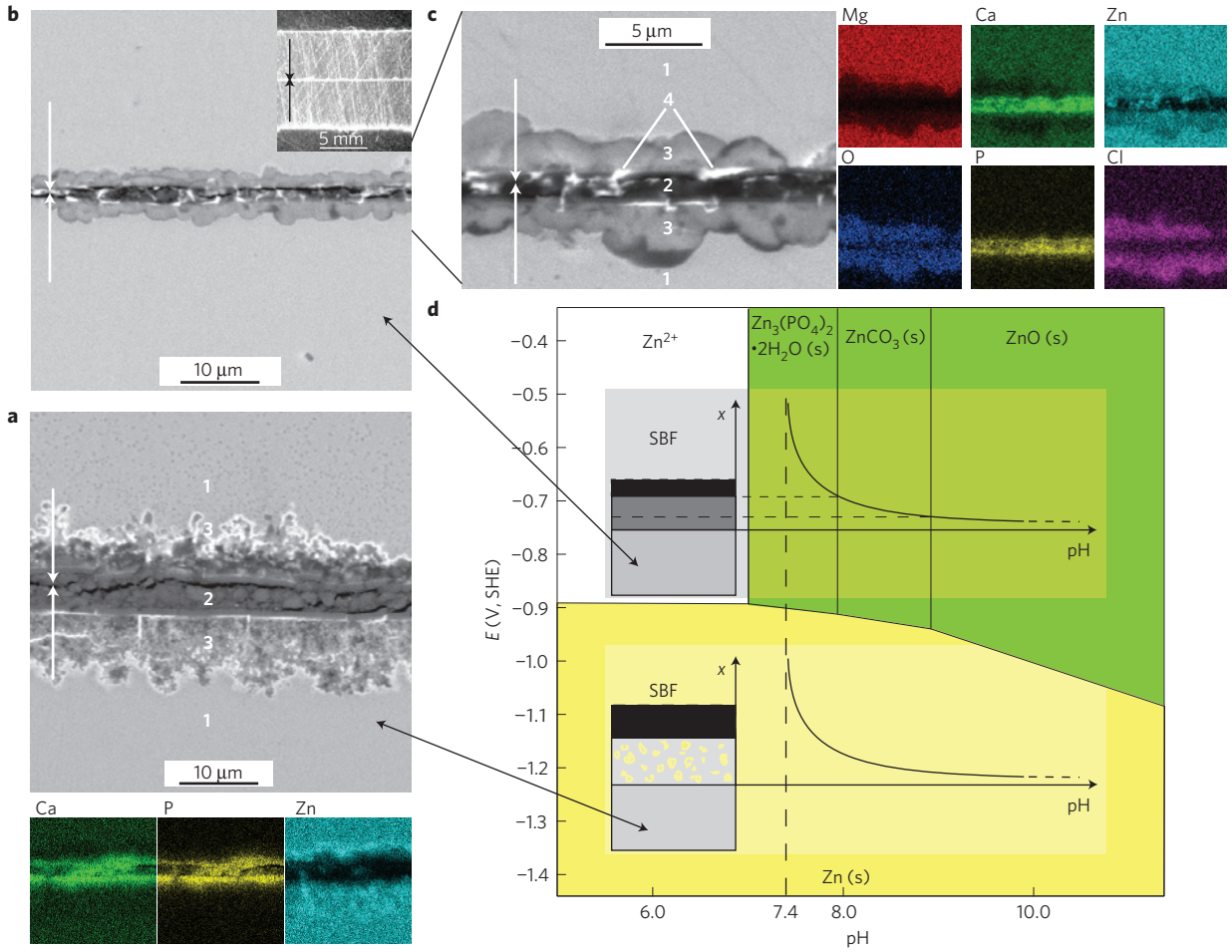

Figure 2 | SEM micrographs of surface corrosion and model explaining this corrosion behaviour. a,**b**, Cross-sections from stacks of immersed plates, where the corrosion surfaces of two samples were stacked surface-to-surface on top of each other and embedded in Bakelite (see inset), for glassy $Mg_{69}Zn_{26}Ca_5$ (**a**) and glassy $Mg_{60}Zn_{35}Ca_5$ (**b**), with white arrows pointing to the sample surfaces. After 72 h of immersion in SBF, a thick (≈10 µm) porous corrosion surface is observed for $Mg_{69}Zn_{26}Ca_5$, whereas a thin (≈3 µm) dense one evolves for $Mg_{60}Zn_{35}Ca_5$. The three EDX maps below **a** demonstrate the occurrence of Ca, P and Zn in the corrosion layers of **a**. **c**, Close-up and corresponding EDX maps of the corrosion surface shown in **b**. **d**, Model explaining the formation of corrosion layers and their dependence on surface potential and local pH, based on the calculated Pourbaix diagram of Zn in contact with SBF. Insets: Assumed pH variation on the sample surface due to Mg dissolution.

Figure 2 shows scanning electron microscope (SEM) images of stacks of MgZnCa plates, immersed for 72 h in SBF, for glassy $Mg_{69}Zn_{26}Ca_5$ (Fig. 2a) and $Mg_{60}Zn_{35}Ca_5$ (Fig. 2b,c). The images reveal significantly different surface structures for the Zn-poor and Zn-rich glasses. A porous, roughly 10-µm-thick, corrosion surface is observed for the hydrogen-evolving, Zn-poor $Mg_{69}Zn_{26}Ca_5$ glass. Electron dispersive X-ray (EDX) analysis reveals the chemical compositions of the two observable layers: the outermost layer (labelled '2') consists mainly of Ca and P, whereas the subjacent one ('3') is enriched in Zn. In contrast, the marginal-hydrogen-evolving $Mg_{60}Zn_{35}Ca_5$ sample in Fig. 2b shows a thin (≈3 µm), dense corrosion surface. A close-up image as shown in Fig. 2c and the corresponding EDX analysis reveal that there are also two separate corrosion layers in this sample: whereas the outermost layer 2 is again rich in Ca and P, the layer 3 adjacent to the bulk material ('1') is rich in Zn and oxygen. The bright non-continuous phases ('4') seen in the SEM image in Fig. 2c are crystalline $CaZn_{13}$ phases (see below). Chloride ions may have a role in the formation of the surface layer because they are also enriched in layer 3.

Figure 3 shows X-ray diffraction (XRD) spectra of the samples $Mg_{60}Zn_{35}Ca_5$, $Mg_{67}Zn_{28}Ca_5$ and $Mg_{74}Zn_{21}Ca_5$ after immersion in SBF for various periods. The samples before immersion (see XRD spectrum at the bottom of Fig. 3) show a typical amorphous structure, whereas clear Bragg peaks are visible after immersion of the samples in SBF. However, although crystalline Zn is observed in $Mg_{74}Zn_{21}Ca_5$, it is not found in the Zn-rich samples, where only Bragg peaks resulting from $CaZn_{13}$ appear. Together with the EDX analysis (Fig. 2), this provides clear evidence of a change in surface condition with a change in the Zn content of the alloys. All samples feature a Ca- and P-rich deposit from the SBF on the outermost layer, and all feature an enrichment of Zn owing to Mg-dealloying in the subjacent layer, but the latter's thickness and morphology are significantly different. In $Mg_{74}Zn_{21}Ca_5$ porous crystalline Zn is present, whereas in the Zn-rich (≥28 at.%) alloys a dense, amorphous Zn- and oxygen-rich layer has formed.

We explained this corrosion behaviour by developing a model based on the Pourbaix diagram of Zn (the main alloying element) calculated for immersion in SBF, using Corrosion Analyzer software (OLIsystems; www.olisystems.com/olicorrosion.htm), and taking into account all of the thermodynamic equilibrium equations of Zn with the ions present in SBF. As can be seen in Fig. 2d, at low potentials ($E < -1.05$ V, as for the gas-evolving $Mg_{75}Zn_{20}Ca_5$ glass; see Fig. 1d), Zn is always in the immunity region (indicated in yellow) and thus stable in its metallic form. At higher surface potentials ($E > -0.9$ V, as for the Zn-rich, marginal-gas-evolving glasses) and pH ≥ 7.4 (the latter is the pH value of human blood),

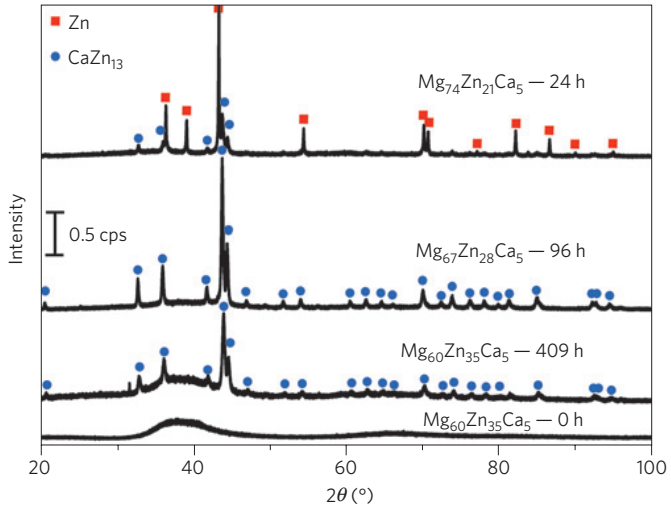

Figure 3 | XRD spectra of glassy $Mg_{60}Zn_{35}Ca_5$, $Mg_{67}Zn_{28}Ca_5$ and $Mg_{74}Zn_{21}Ca_5$ alloys after immersion in SBF for various periods. Bottom curve: XRD image before immersion showing two humps, indicating the amorphous structure of the $Mg_{60}Zn_{35}Ca_5$ sample. Middle curves: XRD images after 409 h of immersion for $Mg_{60}Zn_{35}Ca_5$ and after 96 h of immersion for $Mg_{67}Zn_{28}Ca_5$, showing clear Bragg peaks produced by a crystalline $CaZn_{13}$ phase. These two alloys were immersed longer in SBF than the Zn-rich MgZnCa glass used for SEM investigations (Fig. 2), because, owing to the slow degradation rate, no phase identification was possible by means of XRD after 72 h. Upper curve: XRD image after 24 h of immersion for a Zn-poor MgZnCa glass where severe degradation occurred. Two crystalline phases (Zn and $CaZn_{13}$) could be clearly identified.

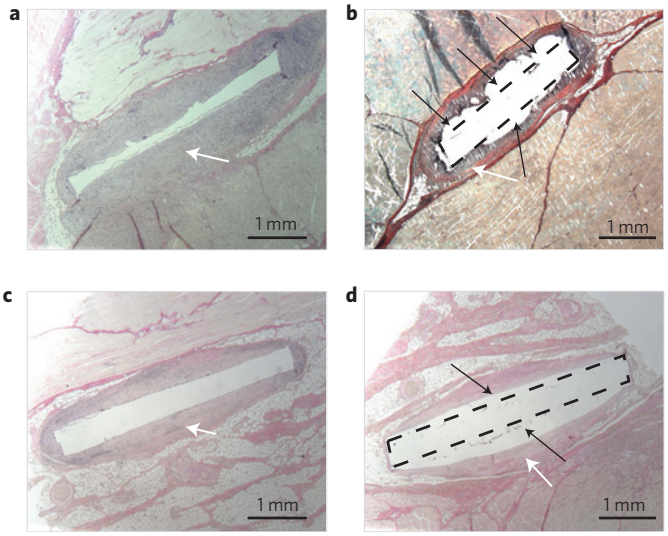

Figure 4 | Animal studies of Mg-based glass in comparison with a crystalline Mg alloy reference sample. a–d, Glassy $Mg_{60}Zn_{35}Ca_5$ (**a**,**c**) and crystalline Mg alloy reference (WZ21) (**b**,**d**) in two types of porcine abdominal tissue (muscle after 27 days (**a**,**b**) and subcutis after 91 days (**c**,**d**) of implantation). All samples show a typical fibrous capsule foreign-body reaction (indicated by white arrows), but only the crystalline samples (implanted discs indicated by dashed lines) show pronounced hydrogen evolution (area between discs and fibrous capsules indicated by black arrows).

Zn is in its non-inert state (indicated in green), and thus forms solid Zn- and oxygen-rich layers. (Note that at pH < 7, Zn would go into solution; see the white area.) On the other hand, in the intermediate region of $-1.05\,V \leq E \leq 0.9\,V$, Zn is able to form solid corrosion layers if the pH value is sufficiently high.

On the basis of the Pourbaix diagram, we thus obtain the following model for the degradation sequence of the MgZnCa samples: at the outset of immersion all alloys show some hydrogen gas evolution, which is caused by Mg dissolution and results in Zn-enrichment of the outermost domain (Mg-dealloying). As immersion progresses, the Zn-poor glasses in the immunity region show monotonous growth of a porous metallic Zn layer (Fig. 2a, layer 3) with hydrogen formation; another indication of this is the increasing OCP over long periods (Fig. 1d). In contrast, the Zn-rich MgZnCa glasses in the active region form a protective layer. As Mg dissolution accompanies a pH increase in the media, the local pH increases in the vicinity of the sample surface. An assumption of the local pH variation, as shown in the model in Fig. 2d, illustrates that with a strong increase in pH a ZnO and/or $ZnCO_3$ protective layer forms. This layer is dense (see Fig. 2c, layer 3) and amorphous (as it was not observed in XRD), and is considered to be responsible for the ebb in hydrogen gas evolution. The deposition of calcium phosphate to build an amorphous permeable layer (Fig. 2a,c, layer 2) is known to occur during immersion in SBF (ref. 30).

Animal studies were carried out in the abdominal walls and cavities (two tissue types apiece) of domestic pigs to evaluate the tissue reactions of the Mg glass during degradation and the hydrogen evolution *in vivo*. Glassy $Mg_{60}Zn_{35}Ca_5$ discs, together with a crystalline reference Mg alloy (WZ21; ref. 31), were implanted and analysed after 27 and 91 days. Figure 4 shows the results of the amorphous and crystalline alloys for the two abdominal wall tissues, muscle and subcutis (liver and omentum are not shown). Around both materials a fibrous capsule, typical of wound-healing processes after implant surgery, has developed in all four different tissue types (see the white arrows). Within the capsules, however, gas cavities formed by hydrogen evolution (as indicated by the black arrows in Fig. 4b,d) are only observed around the crystalline Mg discs. In contrast, no tissue-imprinted hydrogen gas cavities have formed in the histological preparations of the glassy $Mg_{60}Zn_{35}Ca_5$ samples (see Fig. 4a,c). Hence, the *in vivo* tests confirm the findings of the *in vitro* experiments, where no hydrogen evolution was detected for the $Mg_{60}Zn_{35}Ca_5$ glass. Moreover, as no inflammatory reaction was observed for any of the implants, the animal tests show that the $Mg_{60}Zn_{35}Ca_5$ glass shows the same good biocompatibility as the crystalline Mg alloy reference.

We have identified a biodegradable Mg implant material that, owing to the extended solubility of Zn in the amorphous structure of the MgZnCa glass, shows only marginal hydrogen evolution during *in vitro* and *in vivo* degradation. The great reduction in hydrogen evolution by the use of glassy Mg alloys, which this study reports for the first time, represents a significant step towards the use of Mg in biodegradable implants. The further adequate tissue healing seen in conjunction with these alloys, and their high mechanical strength, render the Zn-rich $Mg_{60+x}Zn_{35-x}Ca_5$ $(0 \leq x \leq 7)$ glasses investigated here ideal candidates for biodegradable implant applications.

Methods

High-purity elements (99.5% Ca, 99.99% Mg and 99.99% Zn) were used to cast rods of MgZnCa alloys and the reference materials (pure Mg and $Mg_{98}Zn_2$) from an inductively heated graphite crucible into a copper mould of 12 mm diameter under a high-purity argon atmosphere (99.999%). The MgZnCa precursor material was melt-spun into glassy ribbons of about 50 μm thickness in a helium atmosphere (99.999%). Furthermore, 0.5-mm-thick glassy plates were produced by copper mould injection-casting under an argon atmosphere.

All corrosion measurements were conducted at room temperature at pH 7.3–7.4 in SBF using the same composition as described in ref. 29 for SBF27, but without NaN_3. Hydrogen evolution experiments[16] were carried out by immersing polished ribbons and plates of $Mg_{60+x}Zn_{35-x}Ca_5$ with $x = 0$, 3, 6, 7, 9, 12, 14, 15 and slices of the crystalline reference samples for four days in 200 ml solution per sample.

For electrochemical characterization (OCP, potentiodynamic measurements and EIS) an AUTOLAB/PGSTAT302 system with a FRA2 module was used in a three-electrode set-up with a standard calomel electrode (SCE) and saturated KCl. All tests were conducted on ribbon samples except for EIS, where plates were measured because of the method's high sensitivity. The tests were carried out in 600 ml cm^{-2} SBF; pH changes due to the dissolution of Mg were below 0.4 for all measurements.

A CAMSCAN SEM Series 4 with a NORAN Instruments EDX detector was deployed to image the sample cross-sections and to create EDX maps. XRD measurements were carried out using monochromatic Cu Kα radiation in the Bragg–Brentano geometry with a fixed incoming angle of 20° and a 140° image-plate detector (Stoe, IP-PSD).

Animal tests were carried out at the LEBAO–Medimplant Labor HTTG Hannover according to local regulations and approved by the animal care committee. Discs with a diameter of 4 mm and a thickness of 0.4 mm were sterilized and implanted into two different organs in the abdominal cavity (liver, omentum) and two types of abdominal wall tissue (musculus rectus abdominis, subcutis) in two domestic pigs, and histologically analysed after 27 and 91 days of implantation.

Received 28 May 2009; accepted 21 August 2009; published online 27 September 2009

References

1. Erne, P., Schier, M. & Resink, T. J. The road to bioabsorbable stents: Reaching clinical reality? *Cardiovasc. Inter. Rad.* **29,** 11–16 (2006).
2. Witte, F. *et al. In vitro* and *in vivo* corrosion measurements of magnesium alloys. *Biomaterials* **27,** 1013–1018 (2006).
3. Song, G. L. & Atrens, A. Understanding magnesium corrosion—a framework for improved alloy performance. *Adv. Eng. Mater.* **5,** 837–858 (2003).
4. Scully, J. R., Gebert, A. & Payer, J. H. Corrosion and related mechanical properties of bulk metallic glasses. *J. Mater. Res.* **22,** 302–313 (2007).
5. Staiger, M. P., Pietak, A. M., Huadmai, J. & Dias, G. Magnesium and its alloys as orthopaedic biomaterials: A review. *Biomaterials* **27,** 1728–1734 (2006).
6. Heublein, B. *et al.* Biocorrosion of magnesium alloys: A new principle in cardiovascular implant technology? *Heart* **89,** 651–656 (2003).
7. Erbel, R. *et al.* Temporary scaffolding of coronary arteries with bioabsorbable magnesium stents: A prospective, non-randomised multicentre trial. *Lancet* **369,** 1869–1875 (2007).
8. Hermawan, H., Alamdari, H., Mantovani, D. & Dubé, D. Iron–manganese: New class of metallic degradable biomaterials prepared by powder metallurgy. *Powder Metall.* **51,** 38–45 (2008).
9. Peuster, M. *et al.* Long-term biocompatibility of a corrodible peripheral iron stent in the porcine descending aorta. *Biomaterials* **27,** 4955–4962 (2006).
10. McBride, E. D. Magnesium screw and nail transfixation in fractures. *South. Med. J.* **31,** 508–515 (1938).
11. Verbrugge, J. La tolérance du tissu osseux vis-à-vis du magnésium métallique. *Presse Méd.* **55,** 1112–1114 (1933).
12. Verbrugge, J. Le matériel métallique résorbable en chirurgie osseuse. *Presse Méd.* **23,** 460–465 (1934).
13. Witte, F. *et al. In vivo* corrosion of four magnesium alloys and the associated bone response. *Biomaterials* **26,** 3557–3563 (2005).
14. Peeters, P., Bosiers, M., Verbist, J., Deloose, K. & Heublein, B. Preliminary results after application of absorbable metal stents in patients with critical limb ischemia. *J. Endovasc. Ther.* **12,** 1–5 (2005).
15. Di Mario, C. *et al.* Drug-eluting bioabsorbable magnesium stent. *J. Interv. Cardiol.* **17,** 391–395 (2004).
16. Song, G. L., Atrens, A. & StJohn, D. in *Magnesium Technol.* (ed. Hryn, J. N.) 255–262 (TMS, 2001).
17. Song, G. L. & Atrens, A. Corrosion mechanisms of magnesium alloys. *Adv. Eng. Mater.* **1,** 11–33 (1999).
18. Inoue, A. in *Bulk Amorphous Alloys, Preparation and Fundamental Characteristics* (eds Magini, M. & Wohlbier, F. H.) (Trans Tech Publications, 1998).
19. Johnson, W. L. Bulk glass-forming metallic alloys: Science and technology. *MRS Bull.* **24,** 42–56 (1999).
20. Löffler, J. F. Bulk metallic glasses. *Intermetallics* **11,** 529–540 (2003).
21. Greer, A. L. & Ma, E. Bulk metallic glasses: At the cutting edge of metals research. *MRS Bull.* **32,** 611–615 (2007).
22. Li, Y. *et al.* Formation of bulk metallic glasses and their composites. *MRS Bull.* **32,** 624–628 (2007).
23. Greer, A. L. Metallic glasses... on the threshold. *Mater. Today* **12,** 14–22 (2009).
24. Gu, X., Shiflet, G. J., Guo, F. Q. & Poon, S. J. Mg–Ca–Zn bulk metallic glasses with high strength and significant ductility. *J. Mater. Res.* **20,** 1935–1938 (2005).
25. Zhao, Y. Y., Ma, E. & Xu, J. Reliability of compressive fracture strength of Mg–Zn–Ca bulk metallic glasses: Flaw sensitivity and Weibull statistics. *Scr. Mater.* **58,** 496–499 (2008).
26. Zberg, B., Arata, E. R., Uggowitzer, P. J. & Löffler, J. F. Tensile properties of glassy MgZnCa wires and reliability analysis using Weibull statistics. *Acta Mater.* **57,** 3223–3231 (2009).
27. Hänzi, A. C. *et al.* Design strategy for microalloyed ultra-ductile magnesium alloys. *Phil. Mag. Lett.* **89,** 377–390 (2009).
28. Löffler, J. F., Kündig, A. A. & Dalla Torre, F. H. in *Materials Processing Handbook* (eds Groza, J. R., Shackelford, J. F., Lavernia, E. J. & Powers, M. T.) (CRC Press, 2007).
29. Müller, L. & Müller, F. A. Preparation of SBF with different HCO_3^- content and its influence on the composition of biomimetic apatites. *Acta Biomater.* **2,** 181–189 (2006).
30. Rettig, R. & Virtanen, S. Composition of corrosion layers on a magnesium rare-earth alloy in simulated body fluids. *J. Biomed. Mater. Res. A* **88A,** 359–369 (2009).
31. Hänzi, A. C., Sologubenko, A. S. & Uggowitzer, P. J. Design strategy for new bioabsorbable Mg–Y–Zn alloys for medical applications. *Int. J. Mater. Res.* **100,** 1127–1136 (2009).

Acknowledgements

The authors are grateful for the support of the Swiss Innovation Promotion Agency (CTI Project 7616.2 LSPP-LS).

Author contributions

B.Z. was responsible for the experimental work. P.J.U. and J.F.L. designed the research and J.F.L. supervised the project. All authors contributed to the interpretation of the results and to the writing of the paper.

Additional information

Reprints and permissions information is available online at http://npg.nature.com/reprintsandpermissions. Correspondence and requests for materials should be addressed to J.F.L.